Determination of few femtosecond to attosecond electron bunch durations using a passive plasma lens

Andreas Seidel [1,2,3,*] Carola Zepter [1,2] Alexander Sävert [1,2,3] Stephan Kuschel [4,†] and Matt Zepf [1,2,3]

[1] *Institut für Optik und Quantenelektronik, Friedrich-Schiller-Universität, Fürstengraben 1, 07743 Jena, Germany*

[2] *Helmholtz-Institut Jena, Fröbelstieg 3, 07743 Jena, Germany*

[3] *GSI GmbH, Planckstraße 1, 64291 Darmstadt, Germany*

[4] *Institut für Kernphysik, Technische Universität Darmstadt, Karolinenplatz 5, 64289 Darmstadt, Germany*

(Received 1 July 2025; accepted 23 February 2026; published 7 May 2026)

Determining the pulse duration of femtosecond electron bunches is challenging and often experimentally invasive. An effective method for measuring the duration based on the time-dependent variations in electron beam divergence induced by a passive plasma lens is described. Reconstruction of the temporal shape of the electron bunch down to $c \times dt = 10\,\text{nm}$ ($\sim$30 as) without external RF cavities or multioctave spanning spectrometer is shown numerically. Experimental data from an $\sim$3 fs electron bunch demonstrates practical applicability of this method. While this approach can be used with any high-current electron beam, it is particularly well suited to laser-driven and particle-driven wakefield accelerators, which accommodate electron beams with a time-dependent beam energy (e.g., "chirp").

DOI: 10.1103/zj11-6zxc

I. INTRODUCTION

Laser wakefield acceleration (LWFA) [1] has emerged as a technique capable of generating GeV-class electron beams [2] with femtosecond-scale durations [3] and kiloampere-level peak currents [4]. These ultrashort, high-charge-density bunches enable applications ranging from compact free-electron lasers [5], hybrid acceleration [6] toward future high-energy physics experiments [7], or use LWFA as an injector to replenish a synchrotron [8].

Despite rapid progress, resolving the temporal structure of ultrafast electron bunches, particularly for durations below $\tau < 10\,\text{fs}$, still remains a challenge. Typical accelerator diagnostics, such as x-band radio-frequency cavities [9,10], THz streaking [11], and optical streaking [12], face resolution limits at 10 [13], 1.5, and 1.2 fs, respectively, and require temporal synchronization. Faraday rotation probes [14] struggle with signal-to-noise ratios at sub-10 fs scales. Multioctave spectrometers can provide a measurement of the temporal substructure of the electron bunch on the scale from 0.7 to 40 fs [3], but they are challenging to set up, operate, and require iterative Fourier-based reconstruction algorithms, which deduce the bunch shape from the reconstructed phase.

Plasma lenses are a distinct and new class of electron bunch diagnostic. Active plasma lenses, for example, have been used to measure the emittance [15]. Unlike magnetic lenses, active plasma lenses provide kT/m-scale focusing gradients while simultaneously acting as temporal diagnostic tools. Their chromatic properties enable emittance characterization [16] down to a micrometer-scale level. However, alignment sensitivity has a crucial impact on the measurement [17].

Here, we discuss the use of passive plasma lenses as a pulse duration diagnostic. Passive plasma lensing offers a disruptive alternative to determining electron bunch parameters by exploiting inherent beam-plasma interactions without the need for fine alignment. The extremely rapid response of a passive plasma lens at sufficiently high density offers excellent temporal resolution. In vacuum, a relativistic electron bunch creates magnetic (B_θ) and electric (E_r) fields. The resulting focusing (cB_θ) and defocusing (E_r) forces cancel in the ultrarelativistic limit ($\gamma \to \infty$), such that $E_r - cB_\theta \to 0$.

When a relativistic electron bunch passes through a plasma, two distinct regimes govern the dynamics: the overdense regime ($n_p > n_b$), where the plasma density (n_p) exceeds the density of the electron bunch (n_b), and the underdense regime ($n_p < n_b$). Self-focusing is possible in both regimes. In the overdense regime, the background plasma electrons neutralize the electric field partially, resulting in the focusing of the electron bunch driven by the remaining self-generated magnetic field. Conversely, in the underdense regime, the electron bunch significantly modulates the background plasma density, resulting in strong transverse and longitudinal electromagnetic fields, which in turn generate intense focusing forces on the electron bunch [18–21].

The rapid response of the plasma lens to the temporally varying bunch parameters (particle density, energy chirp) results in spectrally dependent divergence changes. This allows the temporal shape of the electron bunch to be reconstructed with subfemtosecond accuracy

*Contact author: seidel.andreas@uni-jena.de

†Contact author: stephan.kuschel@tu-darmstadt.de

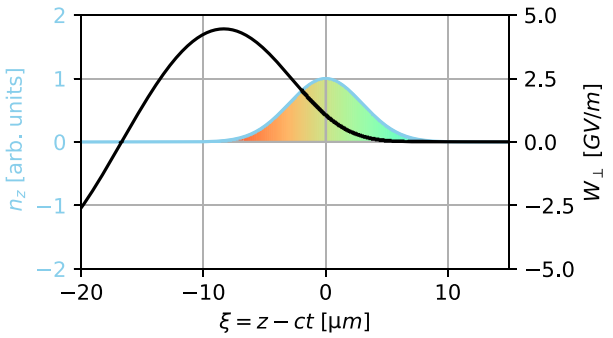

FIG. 1. Analytical transverse wakefield $W_\perp$ from Eq. (1) for a chirped electron bunch with rms beam length $\sigma_z = 3\,\mu m$ and rms beam size $\sigma_r = 6.8\,\mu m$ driving a linear wakefield in a plasma with $n_p = 1 \times 10^{18}\,/\,cm^3$. The total charge of the electron beam is $Q = 65\,pC$. In light blue, the normalized longitudinal charge distribution, and in black, the focusing fields.

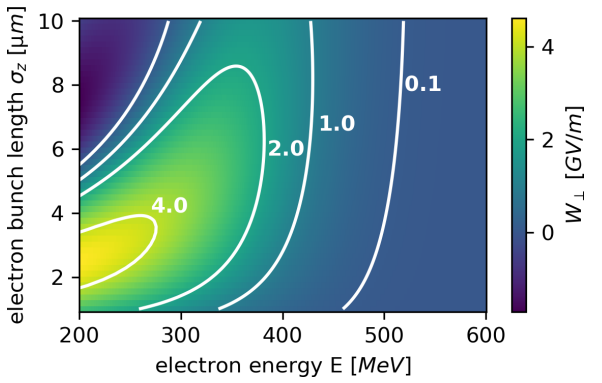

FIG. 2. Analytical result of focusing fields $W_\perp$ from Eq. (1) for different electron bunch lengths. The total charge of the Gaussian electron beam was kept constant at $Q = 65\,pC$. All bunches exhibit a linear energy chirp with $\frac{\partial E}{\partial \xi} = \frac{200\,MeV}{\sigma_z}$, with 400 MeV being located at the center of each bunch ($\xi = z - ct = 0$).

without the need for temporal synchronization or precise alignment.

II. THEORETICAL MODEL

A. Wakefield generation and focusing fields

Transverse wakefields generated by relativistic electron bunches propagating through plasma are analyzed using linear wakefield theory [22,23]. The electron bunch density distribution can be represented as $n_b(\xi = z - ct, r) = n_{b0} \times n_{b||}(\xi) \times n_{b\perp}(r)$, where n_{b0} is the peak charge density, while $n_{b||}$ and $n_{b\perp}$ are the normalized longitudinal and radial charge distributions, respectively. The transverse wakefield, defined as $W_\perp = E_r - cB_\theta$, can be expressed analytically as [Eq. (63) in Ref. [22]]

$$W_\perp(\xi, r) = \frac{-n_{b0} e}{\epsilon_0 k_{pe}} \frac{dR(r)}{dr} \int_{-\infty}^{\xi} n_{b||}(\xi') \times \sin\left(k_{pe}(\xi - \xi')\right) d\xi', \tag{1}$$

where $R(r)$ is given by

$$R(r) = k_{pe}^2 K_0(k_{pe} r) \int_0^r r' n_{b\perp}(r') I_0(k_{pe} r') dr' + k_{pe}^2 I_0(k_{pe} r) \int_r^\infty r' n_{b\perp}(r') K_0(k_{pe} r') dr',$$

with K_0 and I_0 representing modified Bessel functions and k_{pe} the plasma wave number. To prevent beam filamentation, the threshold condition $k_{pe} \times \sigma_r \leqslant 2.2$, with σ_r the transverse root-mean-square (rms) beam size, has been found [24].

The transverse wakefield generated by an electron bunch with $\sigma_z = 3\,\mu m$ is shown in Fig. 1. We assume a chirped electron bunch, as indicated by the color scale. The head of the bunch contains the most energetic electrons, whereas the tail contains the least energetic electrons. Due to the self-induced transverse wakefield, the head of the bunch (the high-energy electrons) experiences weaker focusing fields than the tail (the low-energy electrons). This leads to a significant variation in electron focusing along the bunch's length, resulting in distinct transverse momenta that can be easily measured using magnetic electron spectrometers with angular resolution.

This dependence is shown in Fig. 2: The transverse wakefield strength varies significantly with both electron energy and bunch length. While maintaining a constant charge of 65 pC within a plasma density of $n_p = 1 \times 10^{18}\,/\,cm^3$, we observe that electrons exceeding 500 MeV experience almost no focusing regardless of bunch length. However, at lower energies (250 MeV), the transverse field strength peaks at a bunch length of $\sigma_z = 3\,\mu m$, becoming weaker for both shorter and longer bunches. These distinctive focusing patterns create a unique energy-dependent divergence change in the electron bunch, which enables the reconstruction of the longitudinal bunch profile. The analytical description is valid, when the induced wakefield is in the linear regime, the electron bunch dimensions are smaller than one plasma wavelength, and the electron bunch is monotonically chirped. Its important to note that the actual dependence $E(\xi = z - ct)$ can be modeled and reconstructed with our method as long as it is monotonically increasing or decreasing. The chirp should be large enough to create a sufficiently small slice energy spread at the plasma lens. Through simulations we found that a slice energy spread of more than 10% can reduce the amplitude of the divergence oscillations.

As suggested by the the separatrix model [25], earlier-injected electrons achieve higher energies before reaching dephasing than those injected later, resulting in a broad energy spectrum for bunches generated via ionization injection compared to localized injection mechanisms. Additional positive chirp contributions arise from path length differences during drift—for example, 700 and 100 MeV electrons traveling 100 mm develop a path difference of 1.3 μm, further enhancing the chirp and the observable effects in the energy spectrum.

To quantitatively model the focusing strength experienced by each electron energy inside the electron bunch, we represent the longitudinal electron bunch profile as a sum of discrete, Gaussian-shaped bunchlets, $n_i(\xi_i)$, each with an rms length of 100 nm. These bunchlets contain electrons within a 1 MeV energy interval and are located at longitudinal positions, ξ_i. The total longitudinal profile is then given by $n_{b||}(\xi) = \sum_{i=E_1}^{E_n} n_i(\xi + \xi_i)$. This electron density distribution

generates a wakefield, which in turn produces transverse focusing fields that can be calculated using Eq. (1).

The focusing strength for each bunchlet is characterized by the parameter κ:

$$\kappa(\gamma, \xi) = \frac{e}{p_e} \frac{\partial W_\perp(\xi)}{\partial r}, \tag{2}$$

where $p_e = p_e(\gamma)$ is the momentum of the bunchlet and $\frac{\partial W_\perp(\xi)}{\partial r}$ is the radial derivative of the transverse focusing field. Since each bunchlet $n_i(\xi_i)$ is located at a different longitudinal position, it experiences a distinct focusing wakefield and thus a unique focusing strength parameter $\kappa(\gamma, \xi)$.

B. Transverse beam dynamics

The transverse dynamics of relativistic charged particles can be described using the transfer matrix formalism. For a single particle with initial phase-space coordinates (x_0, x_0'), propagation through an optical system transforms the coordinates

$$\begin{pmatrix} x \\ x' \end{pmatrix} = \tilde{M} \begin{pmatrix} x_0 \\ x_0' \end{pmatrix},$$

where $\tilde{M}$ represents the cumulative transfer matrix formed by multiplying individual component matrices (M_{drift}, M_{lens}, etc.) [26]. In a typical quadrupole lens, the result will have the form of Eq. (3):

$$\tilde{M} = \begin{pmatrix} \cos(\sqrt{\kappa}L) - B\sqrt{\kappa}\sin(\sqrt{\kappa}L) & G\cos(\sqrt{\kappa}L) + \frac{1}{\sqrt{\kappa}}\sin(\sqrt{\kappa}L) + B(-G\sqrt{\kappa}\sin(\sqrt{\kappa}L) + \cos(\sqrt{\kappa}L)) \\ -\sqrt{\kappa}\sin(\sqrt{\kappa}L) & -G\sqrt{\kappa}\sin(\sqrt{\kappa}L) + \cos(\sqrt{\kappa}L) \end{pmatrix}. \tag{3}$$

Here, G and B denote drift lengths before/after the lens, L the quadrupole length, and $\kappa = \frac{1}{Lf_0\gamma/\gamma_0}$ the normalized focusing strength, where f_0 is the reference focal length at energy $\gamma_0 mc^2$. For our plasma lens, this is replaced by Eq. (2).

For a *particle ensemble*, this formalism extends to beam size and divergence via the covariance matrix $\Sigma = \langle \mathbf{X}\mathbf{X}^\top \rangle$, where $\mathbf{X} = (\sigma_0, \sigma_0')^\top$. Under the Courant-Snyder parametrization (α, β, γ) [27], the geometric emittance is conserved as $\epsilon = \sqrt{\det \Sigma}$. Assuming a beam waist ($\alpha = 0$) at the plasma source exit, the final rms beam size at the spectrometer reduces to

$$\sigma_f = \sqrt{\tilde{M}_{11}^2 \sigma_0^2 + \tilde{M}_{12}^2 \sigma_0'^2}, \tag{4}$$

where σ_0 and σ_0' are the initial rms size and divergence. We use this formula to calculate the beam size on the spectrometer screen and the parameter κ is given by the wakefield [Eq. (2)].

III. EXPERIMENT

A. Setup

An experiment was conducted that allowed the temporal response of the passive plasma lens to be tested. The experiment was conducted at the JETi200 laser system at the Helmholtz Institute Jena (setup shown in Fig. 3). The laser system delivered pulses with energies up to $E = 4.0$ J at a central wavelength of $\lambda_0 = 800$ nm and duration of $\tau = 23$ fs. An $f/24$ off-axis parabolic mirror focused the beam to a vacuum full width at half maximum (FWHM) focal spot diameter of 22 µm, with approximately 40% of the total energy contained within the FWHM, resulting in a normalized vector potential of $a_0 = 2.9$.

The laser beam was focused into the entrance of a 7.0-mm-long gas cell, developed at the Helmholtz Institute Jena. It was filled with a 92% helium and 8% nitrogen mixture by volume. The higher nitrogen concentration compared to the commonly used 1%–5% used for ionization injection maximized electron beam charge while maintaining adequate laser guiding. ANSYS [28] fluid dynamics simulations of the gas flow through the cell revealed a central 6-mm-long uniform density region with 1.5-mm-long density ramps on either side.

The secondary target, used for plasma lensing, was a 7-mm-wide Laval nozzle operated with pure helium, positioned at a variable distance between 4 and 125 mm behind the gas cell exit. Interferometric measurements [29] confirmed that the neutral gas density profile above the nozzle remained stable within 5% at a height of 2 mm above the nozzle.

A Kodak BioMAX scintillation screen [30] positioned 237 cm downstream from the gas cell recorded the electron beam profiles and spectra. A 10-cm-long dipole magnet could be inserted into the beam path, allowing for measurement of either the electron beam profile or energy spectrum on the same screen. The optical system was calibrated using a 530 nm laser diode in conjunction with established scintillator response curves [30], enabling absolute charge measurements.

B. Passive plasma lens results

The experimental results of the electron beam energy spectrum after acceleration in the gas cell and subsequent

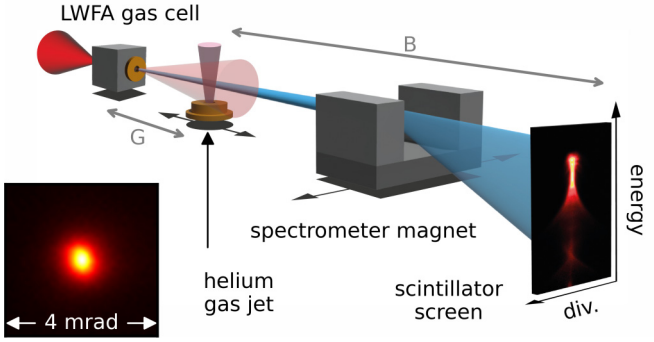

FIG. 3. Schematic of the experimental setup. The JETi200 laser is focused with an $f/24$ parabolic mirror onto a gas cell. The distance between the gas cell and the consecutive jet acting as plasma lens could be varied. A movable dipole magnet disperses the electrons on the scintillation screen, enabling measurement of the energy spectrum and transverse beam profile. Left inset: Transverse beam profile.

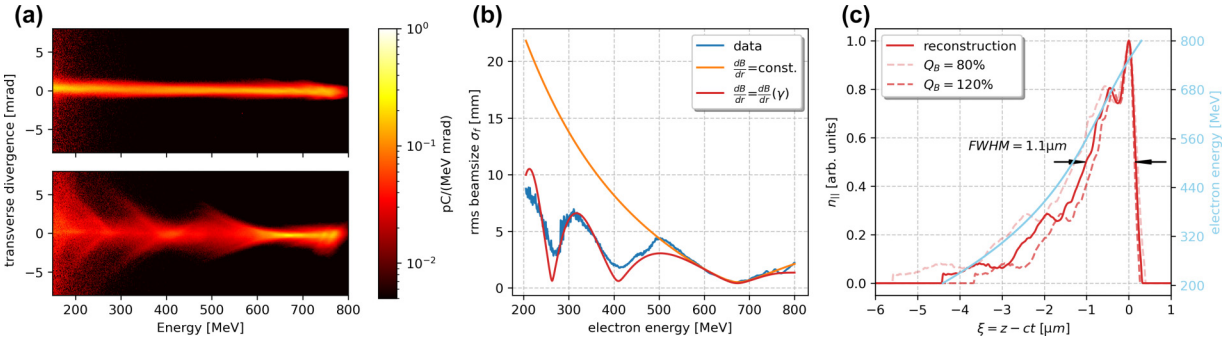

FIG. 4. (a) Observed electron beam energy spectrum without [panel (a), top] and with [panel (a), bottom] plasma lens, showing the transverse divergence as a function of energy. Pronounced modulations in the beam divergence are observed across the spectrum with a plasma lens. (b) Root-mean-square beam size as a function of electron energy. The blue curve represents experimental data extracted from vertical lineouts of the spectrum in panel (a), bottom. The orange and red curves correspond to results from different fitting algorithms, including constant dB/dr (orange) and energy-dependent $dB/dr(\gamma)$ (red). (c) Reconstruction of the longitudinal electron bunch profile corresponding to the analytic model underlying the result in panel (b) (red curve). Dashed curves indicate the solutions obtained assuming different bunch charges with 80% and 120% of nominal bunch charge shown, respectively. In light blue, the electron bunch energy over the position ξ.

propagation through a plasma lens are presented in Fig. 4(a). In this configuration, the distance between the acceleration stage and the plasma lens (second gas jet) was $G = 7$ mm, with the plasma lens itself being 7 mm long and the spectrometer screen positioned $B = 2360$ mm from the plasma lens. The data show clear focusing of the electron beam at energies of 650 and 415 MeV, while significant defocusing is observed at 500 and 310 MeV [see Fig. 4(a), bottom]. Notably, the highest electron energies ($E > 750$ MeV) remain largely unaffected by the plasma lens, as predicted by the theory.

These focusing-defocusing features are more clearly illustrated in Fig. 4(b), where the rms beam size on the screen as a function of electron energy is shown in blue. This panel also compares the experimental data to several theoretical models. Given the precisely known distances in our setup, we apply Eqs. (3) and (4) under the assumption of a constant magnetic field gradient, which is typical for magnetic quadrupole lenses or solenoids, but clearly violated for our plasma lens. The resulting beam size (orange curve) accurately describes the high-energy portion of the spectrum ($E > 500$ MeV), but fails to capture the pronounced oscillations in beam divergence observed at lower energies. Such oscillatory behavior is predicted at much lower electron energies ($E < 50$ MeV) for a constant-gradient lens (see the Supplemental Material [31]). This observation agrees with the prediction, based on wakefield theory, that the electron bunch is positively chirped, meaning that lower-energy electrons are positioned at the rear of the bunch and thus experience stronger focusing fields.

Further including Eq. (2) into the calculation and using the model described earlier, the final beam size on the spectrometer is shown in Fig. 4(b) (red curve). We iteratively adjusted the positions ξ_i of the bunchlets and recalculated the resulting focusing field $W_\perp(\xi)$ and final beam size to minimize the differences between the modeled and the measured transverse beam sizes on the spectrometer. Details of this optimization procedure are provided in the Supplemental Material [32].

The result of this optimization procedure [Fig. 4(b), red curve] exhibits excellent agreement with the experimental data, accurately reproducing both the positions of the minima and maxima in the rms beam size across the entire energy range. The final reconstructed longitudinal bunch profile $n_{b||}(\xi)$, based on the optimized positions ξ_i of all bunchlets, is shown in Fig. 4(c). The dashed lines show the reconstructions with ±20% bunch charge. The reconstructed bunch length is consistent with previous studies [3,14].

C. Comparison of PIC simulation and theoretical reconstruction

We performed particle-in-cell (PIC) simulations using FBPIC [33] to fully model the passive plasma lens interaction. The simulation domain in longitudinal and radial directions was set to 50 μm × 20 μm (3200 × 200 grid points) using $N_m = 2$ azimuthal modes. We simulated an electron bunch with an intitial rms divergence of 0.2 mrad while retaining key parameters of the experiment: (75 pC) charge, a triangular energy spectrum (200–800 MeV, peaking at 750 MeV), rms source size (1 μm), and total bunch length (3 μm). The electron source-to-plasma lens distance was increased to 40 mm (from 7 mm in the experiment (resulting in the same charge density at the plasma lens) and maintaining a total source-to-spectrometer distance of 2370 mm. The lens was modeled with a rectangular density profile ($n_P = 1 \times 10^{17}$ cm^{-3} and $L = 2$ mm), deliberately reducing the focusing field strength $W_\perp$ to suppress multienergy oscillations to test our focusing model.

The parameters chosen for the simulation exhibit a single focus as shown in Fig. 5(a). We find that this improves the fidelity of reconstruction. Applying the analytic model from Fig. 4(b) (red curve) to this configuration yields excellent agreement with the simulation (dashed lines), confirming the model's validity under controlled conditions. The reconstructed longitudinal bunch profile from the analytic reconstruction [Fig. 5(b), dashed lines] aligns closely with the input PIC simulation profiles (solid curves), matching both the total bunch length (3 μm) and the overall shape. This correspondence validates the analytic method's ability to reconstruct longitudinal bunch structures with high fidelity when phase-space perturbations are minimized. The rising

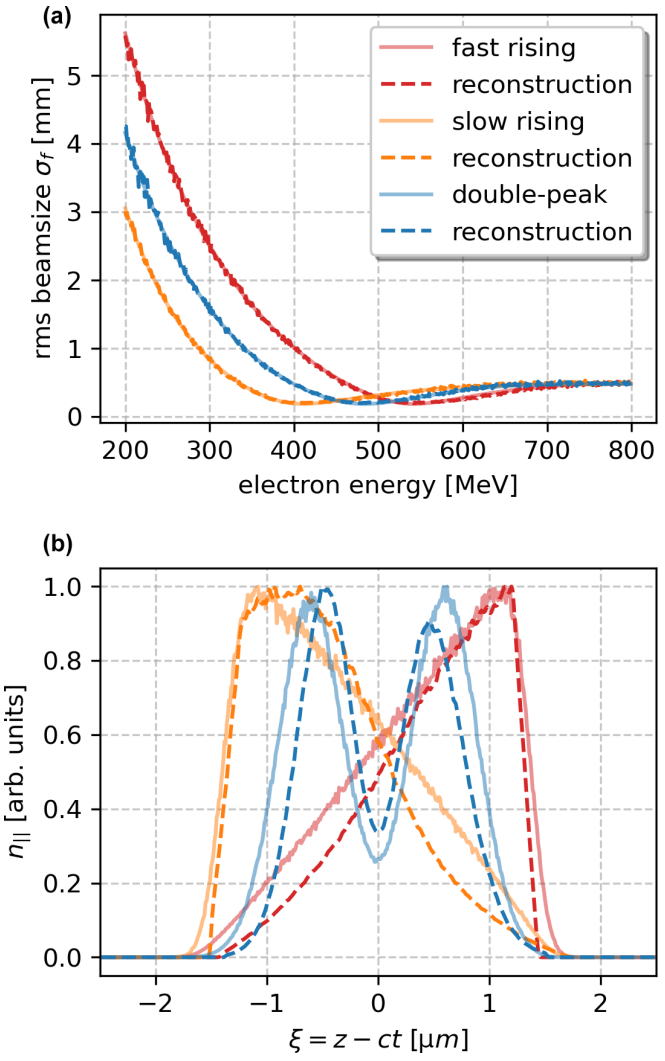

FIG. 5. (a) Root-mean-square beam size as a function of electron energy for electron bunchs with different longitudinal profile after plasma lensing, comparing PIC simulation results (solid) and analytical modeling (dashed) for optimized lens parameters (rectangular density profile, $n_P = 1 \times 10^{17}\,\mathrm{cm}^{-3}$ and $L = 2\,\mathrm{mm}$). (b) Comparison of the reconstructed longitudinal bunch profiles from analytic modeling (dashed) and the profile used as input for the PIC simulation (solid), showing closely matched pulse shape and overall bunch length.

(falling) edge of the pulses in Fig. 5 has a 10%–90% edge of 1 fs (∼300 nm) showing the high temporal resolution obtainable.

We also performed simulations comparing the transverse beam size dynamics for electron bunches ranging from 2 μm to 100 nm (total bunch length, not rms) in order to systematically quantify the impact of bunch length on the electron beam focusing in Fig. 6. All configurations retained the experimental longitudinal plasma density profile and constant electron bunch charge density. For short bunches ($k_p\sigma_z \ll 1$, where $\sigma_z < 3\,\mu\mathrm{m}$; see Fig. 2), wakefield theory predicts weaker transverse focusing fields at the same electron energy due to reduced overlap with the plasma wake. To counteract this, we scaled the plasma lens density inversely with bunch

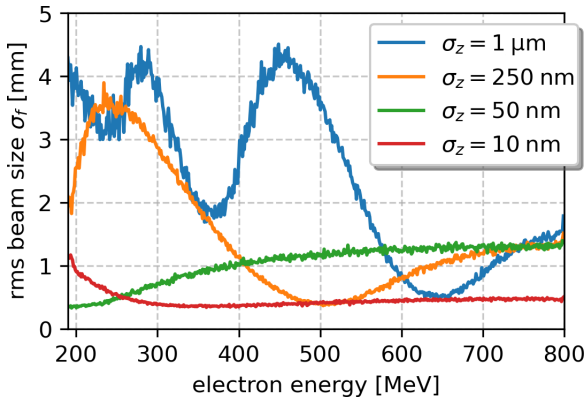

FIG. 6. PIC simulation results of the rms beam size vs electron energy for total bunch lengths ($2\sigma_z$) from 2 μm to 20 nm. The electron bunch charge density is constant for all cases, while the plasma lens density is scaled as $n_P = 8.5 \times 10^{17}\,\mathrm{cm}^{-3} \times \frac{1\,\mu\mathrm{m}}{\sigma_z}$. Shorter bunches exhibit reduced beam size oscillations, due to weaker focusing fields $W_\perp$. The plasma lens profile was changed from Gaussian to rectangular, and the divergence was reduced to 0.2 mrad for the shortest bunch $\sigma_z = 10\,\mathrm{nm}$ to increase focusing while adhering to Ref. [34].

length: $n_P = 8.5 \times 10^{17}\,\mathrm{cm}^{-3} \times \frac{1\,\mu\mathrm{m}}{\sigma_z}$. However, because the charge density of the bunch was held constant in the simulations, shorter bunches caused weaker wakefields, leading to weaker beam focusing. Scalings of the simulations revealed a trade-off: Reducing bunch charge by a factor of 3 necessitated quadrupling the lens' plasma density to maintain similar modulations in the energy spectrum (see the Supplemental Material [34]).

Figure 6 reveals that beam size modulations—critical for longitudinal profile reconstruction—persist across all electron bunches. Strikingly, these modulations remain resolvable even in the subfemtosecond regime (red curve), enabling a direct measurement of bunch lengths deep within the attosecond regime.

IV. CONCLUSION

The rapidly evolving fields of passive plasma lenses have been shown to provide the basis for a powerful diagnostic of femtosecond to attosecond duration electron bunches. This study demonstrates that the energy-dependent electron beam focusing in a plasma lens results in chromatic modulation patterns that encode the longitudinal bunch structure. An analytic model that reconstructs longitudinal bunch profiles from these modulations is presented and validated through PIC simulations for both chirped and unchirped pulses. Highest sensitivity depends on choosing the correct plasma lens density and length.

The analytical reconstruction methodology benefits from the broad energy bandwidths characteristic of LWFA electron beams. However, as demonstrated in the Supplemental Material [35], distinct divergence modulation patterns persist for bandwidths as narrow as 20 MeV. For significantly narrower bandwidths, the reconstruction method would require extension to account for longitudinal acceleration. Finally, while the analytic model is derived assuming linear wakefields with negligible plasma density perturbation, the reconstruc-

tion proves robust even in the underdense interaction regime ($n_b \gg n_p$), as confirmed by the agreement with PIC simulations shown in Fig. 5.

ACKNOWLEDGMENTS

The authors thank G. Schäfer for operating the JETi200 laser system. This work was also funded by the Deutsche Forschungsgemeinschaft (DFG, German Research Foundation) under Project No. 392856280.

DATA AVAILABILITY

The data that support the findings of this article are openly available [36].

[1] T. Tajima and J. M. Dawson, Laser electron accelerator, Phys. Rev. Lett. **43**, 267 (1979).

[2] A. J. Gonsalves, K. Nakamura, J. Daniels, C. Benedetti, C. Pieronek, T. C. H. de Raadt, S. Steinke, J. H. Bin, S. S. Bulanov, J. van Tilborg, *et al.*, Petawatt laser guiding and electron beam acceleration to 8 GeV in a laser-heated capillary discharge waveguide, Phys. Rev. Lett. **122**, 084801 (2019).

[3] O. Zarini, J. C. Cabadağ, Y.-Y. Chang, A. Köhler, T. Kurz, S. Schöbel, W. Seidel, M. Bussmann, U. Schramm, A. Irman, and A. Debus, Multioctave high-dynamic range optical spectrometer for single-pulse, longitudinal characterization of ultrashort electron bunches, Phys. Rev. Accel. Beams **25**, 012801 (2022).

[4] K. Huang, Z. Jin, N. Nakanii, T. Hosokai, and M. Kando, Electro-optic 3D snapshot of a laser wakefield accelerated kiloampere electron bunch, Light: Sci. Appl. **13**, 84 (2024).

[5] M. Galletti, R. Assmann, M. E. Couprie, M. Ferrario, L. Giannessi, A. Irman, R. Pompili, and W. Wang, Prospects for free-electron lasers powered by plasma-wakefield-accelerated beams, Nat. Photonics **18**, 780 (2024).

[6] B. Hidding, R. Assmann, M. Bussmann, D. Campbell, Y.-Y. Chang, S. Corde, J. C. Cabadağ, A. Debus, A. Döpp, M. Gilljohann, *et al.*, Progress in hybrid plasma wakefield acceleration, Photonics **10**, 99 (2023).

[7] B. Foster, R. D'Arcy, and C. A. Lindstrøm, A hybrid, asymmetric, linear Higgs factory based on plasma-wakefield and radio-frequency acceleration, New J. Phys. **25**, 093037 (2023).

[8] S. A. Antipov, A. F. Pousa, I. Agapov, R. Brinkmann, A. R. Maier, S. Jalas, L. Jeppe, M. Kirchen, W. P. Leemans, A. M. de la Ossa, J. Osterhoff, M. Thévenet, and P. Winkler, Design of a prototype laser-plasma injector for an electron synchrotron, Phys. Rev. Accel. Beams **24**, 111301 (2021).

[9] C. Behrens, F.-J. Decker, Y. Ding, V. A. Dolgashev, J. Frisch, Z. Huang, P. Krejcik, H. Loos, A. Lutman, T. J. Maxwell, J. Turner, J. Wang, M.-H. Wang, J. Welch, and J. Wu, Few-femtosecond time-resolved measurements of X-ray free-electron lasers, Nat. Commun. **5**, 3762 (2014).

[10] V. A. Dolgashev, G. Bowden, Y. Ding, P. Emma, P. Krejcik, J. Lewandowski, C. Limborg, M. Litos, J. Wang, and D. Xiang, Design and application of multimegawatt x-band deflectors for femtosecond electron beam diagnostics, Phys. Rev. Spec. Top. Accel. Beams **17**, 102801 (2014).

[11] L. Zhao, Z. Wang, C. Lu, R. Wang, C. Hu, P. Wang, J. Qi, T. Jiang, S. Liu, Z. Ma, *et al.*, Terahertz streaking of few-femtosecond relativistic electron beams, Phys. Rev. X **8**, 021061 (2018).

[12] M. Kozák, J. McNeur, K. J. Leedle, H. Deng, N. Schönenberger, A. Ruehl, I. Hartl, J. S. Harris, R. L. Byer, and P. Hommelhoff, Optical gating and streaking of free electrons with sub-optical cycle precision, Nat. Commun. **8**, 14342 (2017).

[13] J. Maxson, D. Cesar, G. Calmasini, A. Ody, P. Musumeci, and D. Alesini, Direct measurement of sub-10 fs relativistic electron beams with ultralow emittance, Phys. Rev. Lett. **118**, 154802 (2017).

[14] A. Buck, M. Nicolai, K. Schmid, C. M. S. Sears, A. Sävert, J. M. Mikhailova, F. Krausz, M. C. Kaluza, and L. Veisz, Real-time observation of laser-driven electron acceleration, Nat. Phys. **7**, 543 (2011).

[15] S. K. Barber, J. H. Bin, A. J. Gonsalves, F. Isono, J. van Tilborg, S. Steinke, K. Nakamura, A. Zingale, N. A. Czapla, D. Schumacher, C. B. Schroeder, C. G. R. Geddes, W. P. Leemans, and E. Esarey, A compact, high resolution energy, and emittance diagnostic for electron beams using active plasma lenses, Appl. Phys. Lett. **116**, 234108 (2020).

[16] S. K. Barber, J. V. Tilborg, C. B. Schroeder, R. Lehe, H. E. Tsai, K. K. Swanson, S. Steinke, K. Nakamura, C. G. R. Geddes, C. Benedetti, E. Esarey, and W. P. Leemans, Measured emittance dependence on the injection method in laser plasma accelerators, Phys. Rev. Lett. **119**, 104801 (2017).

[17] C. A. Lindstrøm, E. Adli, G. Boyle, R. Corsini, A. E. Dyson, W. Farabolini, S. M. Hooker, M. Meisel, J. Osterhoff, J.-H. Röckemann, L. Schaper, and K. N. Sjobak, Emittance preservation in an aberration-free active plasma lens, Phys. Rev. Lett. **121**, 194801 (2018).

[18] S. Kuschel, D. Hollatz, T. Heinemann, O. Karger, M. B. Schwab, D. Ullmann, A. Knetsch, A. Seidel, C. Rödel, M. Yeung, M. Leier, A. Blinne, H. Ding, T. Kurz, D. J. Corvan, A. Sävert, S. Karsch, M. C. Kaluza, B. Hidding, and M. Zepf, Demonstration of passive plasma lensing of a laser wakefield accelerated electron bunch, Phys. Rev. Accel. Beams **19**, 071301 (2016).

[19] C. Thaury, E. Guillaume, A. Döpp, R. Lehe, A. Lifschitz, K. Ta Phuoc, J. Gautier, J.-P. Goddet, A. Tafzi, A. Flacco, F. Tissandier, S. Sebban, A. Rousse, and V. Malka, Demonstration of relativistic electron beam focusing by a laser-plasma lens, Nat. Commun. **6**, 6860 (2015).

[20] C. E. Doss, E. Adli, R. Ariniello, J. Cary, S. Corde, B. Hidding, M. J. Hogan, K. Hunt-Stone, C. Joshi, K. A. Marsh, J. B. Rosenzweig, N. Vafaei-Najafabadi, V. Yakimenko, and M. Litos, Laser-ionized, beam-driven, underdense, passive thin plasma lens, Phys. Rev. Accel. Beams **22**, 111001 (2019).

[21] C. E. Doss, R. Ariniello, J. R. Cary, S. Corde, H. Ekerfelt, E. Gerstmayr, S. J. Gessner, M. Gilljohann, C. Hansel, B. Hidding, M. J. Hogan, A. Knetsch, V. Lee, K. Marsh, B. O'Shea, P. San Miguel Claveria, D. Storey, A. Sutherland, C. Zhang, and M. D. Litos, Underdense plasma lens with a transverse density gradient, Phys. Rev. Accel. Beams **26**, 031302 (2023).

[22] R. Keinigs and M. E. Jones, Two-dimensional dynamics of the plasma wakefield accelerator, Phys. Fluids **30**, 252 (1987).

[23] L. Verra, Electron bunch seeding of the self-modulation instability in plasma, Ph.D. thesis, Technische Universität München, 2022.

[24] B. Allen, V. Yakimenko, M. Babzien, M. Fedurin, K. Kusche, and P. Muggli, Experimental study of current filamentation instability, Phys. Rev. Lett. **109**, 185007 (2012).

[25] E. Esarey and M. Pilloff, Trapping and acceleration in nonlinear plasma waves, Phys. Plasmas **2**, 1432 (1995).

[26] M. Reiser, *Theory and Design of Charged Particle Beams* (WILEY-VCH Verlag GmbH & Co. KGaA, Weinheim, 2008).

[27] E. D. Courant and H. S. Snyder, Theory of the alternating-gradient synchrotron, Ann. Phys. **3**, 1 (1958).

[28] ANSYS, Inc., ANSYS Fluent User's Guide, version 2019R1, 2019.

[29] M. J. Hüther, Design and characterisation of supersonic nozzles for shock front electron injection in laser wakefield acceleration, Master's thesis, Ludwig-Maximilians-Universität München, 2015.

[30] T. Kurz, J. P. Couperus, J. M. Krämer, H. Ding, S. Kuschel, A. Köhler, O. Zarini, D. Hollatz, D. Schinkel, R. D'Arcy, J.-P. Schwinkendorf, J. Osterhoff, A. Irman, U. Schramm, and S. Karsch, Calibration and cross-laboratory implementation of scintillating screens for electron bunch charge determination, Rev. Sci. Instrum. **89**, 093303 (2018).

[31] See Supplemental Material at http://link.aps.org/supplemental/10.1103/zj11-6zxc for a description of the focusing with constant magnetic field gradient down to an electron energy of 1 MeV.

[32] See Supplemental Material at http://link.aps.org/supplemental/10.1103/zj11-6zxc for a detailed description of the analytic reconstruction of the longitudinal bunch profile.

[33] R. Lehe, M. Kirchen, I. A. Andriyash, B. B. Godfrey, and J.-L. Vay, A spectral, quasi-cylindrical and dispersion-free particle-in-cell algorithm, Comput. Phys. Commun. **203**, 66 (2016).

[34] See Supplemental Material at http://link.aps.org/supplemental/10.1103/zj11-6zxc for guidelines about the correct parameters for the plasma lens with respect to the electron bunch.

[35] See Supplemental Material at http://link.aps.org/supplemental/10.1103/zj11-6zxc for insights on the impact of a short initial bandwidth of 20 MeV of the electron bunch on the bunch-plasma lens interaction.

[36] A. Seidel, C. Zepter, A. Sävert, S. Kuschel, and M. Zepf, Determination of few femtosecond to attosecond electron bunch durations using a passive plasma lens, Zenodo (2025), http://doi.org/10.5281/zenodo.15784529.